Research Article Vol. 33, No. 4 / 24 Feb 2025 / Optics Express 8774
Optics EXPRESS

Membrane optomechanical magnetometer

QIANG ZHANG,[1,2,3] SIMIN DU,[1,2] SHIWEI YANG,[1,2] QUANSEN WANG,[1,2] AND YONGMIN LI[1,2,4]

[1]State Key Laboratory of Quantum Optics and Quantum Optics Devices, Institute of Opto-Electronics, Shanxi University, Taiyuan 030006, China
[2]Collaborative Innovation Center of Extreme Optics, Shanxi University, Taiyuan, Shanxi 030006, China
[3]qzhang@sxu.edu.cn
[4]yongmin@sxu.edu.cn

Abstract: We demonstrate an optomechanical magnetometer where a high-Q membrane mechanical resonator responds to the magnetic-field-induced deformations of two magnetostrictive materials and is monitored by a two-beam Fabry-Perot cavity. The magnetometer enables simultaneous measurements of DC and AC magnetic fields and can recognize the direction of a two-dimensional DC magnetic field by demodulating the frequency shifts of two nondegenerate modes of the membrane. Benefiting from the two-beam interference and high-Q mechanical resonance, this device does not suffer from the linewidth and polarization fluctuation of the probe light as the reported counterparts, overcoming the dependence of optomechanical magnetometers on ultranarrow-linewidth laser and high-Q optical cavity with frequency locking equipment. This work opens a new avenue for measurements of weak magnetic fields.

1. Introduction

Cavity optomechanics is a versatile platform for both the fundamental physics and ultrasensitive sensors by manipulating the interactions between electromagnetic waves and acoustic resonators [1–5]. Notably, benefiting from the resonant enhancement of both optical and mechanical responses, many outstanding cavity optomechanical sensors have been achieved for various physical quantities [6–34]. Recently, cavity optomechanical magnetometers have attracted extensive attentions for measurement of weak alternating current (AC) magnetic fields [35–44], owing to the unique advantages of room-temperature operation, magnetic shielding free, large frequency range (from kHz to GHz), and high sensitivity. However, they are unsuitable for measurement of direct current (DC) magnetic fields, which generally coexist with AC magnetic fields in most practical application scenarios [45,46]. Thus, it is still an open challenge to simultaneously measure DC and AC magnetic fields for cavity optomechanical magnetometers.

In this work, we demonstrate a magnetometer using a SiN-membrane optomechanical system, enabling the simultaneous measurements of both DC and AC magnetic fields. The observed peak response of DC magnetic field is 1771Hz/Gs, which represents a resolution of 56.5 nT using an electrical spectrum analyzer (ESA) with a 1 Hz resolution bandwidth (*RBW*). That is 530 times better than the best value of 30 μT with whispering gallery mode resonators [47]. Meanwhile, the proposed membrane optomechanical magnetometer can measure the direction of a two-dimensional DC magnetic field by simultaneously monitoring the resonant frequency shifts of (1,2) and (2,1) modes of the membrane resonator, which has never been realized in previous optomechanical magnetometers. In addition, the proposed magnetometer is unsensitive to the linewidth and polarization fluctuation of the probe light as the reported counterparts, overcoming the dependence of optomechanical magnetometers on narrow-linewidth laser and high-Q cavity with frequency locking equipment. This work offers a promising candidate for potential applications, such as archaeology, mineral exploration, geomagnetic anomalies, and space exploration missions.

#550415 https://doi.org/10.1364/OE.550415
Journal © 2025 Received 27 Nov 2024; revised 4 Feb 2025; accepted 4 Feb 2025; published 20 Feb 2025

Optics EXPRESS

2. Principle

The working principle of the optomechanical magnetometer is presented in Fig. 1. As shown in Fig. 1(a), the magnetometer consists of a rectangular SiN membrane (golden yellow), and two Terfenol-D plates magnetized uniaxially (gray), constricted by an aluminum square frame (blue), and a two-beam Fabry-Perot (FP) cavity formed by the end face of a single mode fiber (SMF) and the SiN membrane. The SiN membrane is grown by low-pressure chemical vapor deposition on a 500 μm thick silicon wafer (Norcada Inc.). The two Terfenol-D plates are customized from Huizhou South Rare Earth Functional Material Institute Co. This device is placed in a vacuum chamber with the gas pressure of 10^{-5} mbar for high mechanical Q factor of the SiN membrane. When an ambient magnetic field is applied to the magnetometer, the Terfenol-D plates generate the associated deformation and thus extrude the SiN membrane. Figure 1(b) shows the stress diagram of the SiN membrane with ambient magnetic fields B_x and B_y. Owing to the intrinsical high tensile stress, the SiN membrane offers high-Q mechanical resonances which is ultrasensitive to minute stress fluctuations. The mechanical susceptibility of the membrane resonator is

$$\chi(\omega) = \frac{1}{\omega_{mec}^2 - \omega^2 + i\omega\omega_m/Q_{mec}} \tag{1}$$

where $\omega_{\mathrm{mec}} = 2\pi f_{\mathrm{mn}}$ and Q_{mec} are the resonant angular frequency and quality factor of the mechanical mode (m, n), and the resonant frequency f_{mn} of the rectangular membrane can be expressed as:

$$f_{mn}(\varepsilon) = \sqrt{\frac{(F_0 + \Delta F_x)m^2}{4\rho L_x^2} + \frac{(F_0 + \Delta F_y)n^2}{4\rho L_y^2}}, \tag{2}$$

$$\Delta F_x = E\frac{kB_x L_{TDx}}{L_{SI}} + \beta E\frac{kB_y L_{TDy}}{L_{SI}}, \tag{3}$$

$$\Delta F_y = E\frac{kB_y L_{TDy}}{L_{SI}} + \beta E\frac{kB_x L_{TDx}}{L_{SI}}, \tag{4}$$

where F_0 is the initial tensile stress inside the SiN membrane, ΔF_{i} is the tensile stress arising from the ambient magnetic fields (i is x or y, respectively), ρ is the mass density, $L_{\mathrm{i}} = L_{\mathrm{i0}}$ (1-$\Delta F_{\mathrm{i}}/E$) is side length of the SiN membrane, L_{i0} is initial length of the membrane, E is the Young's modulus of the membrane, L_{Si} is length of the silicon chip, k and L_{TD} are the magnetostrictive coefficient and length of the Terfenol-D plates, β is Poisson's ratio of silicon chip, and B_{i} is the ambient magnetic fields.

A two-beam FP cavity is constructed by the SMF and the membrane to monitor the motion states of the membrane as shown in Fig. 1(a). The normalized reflective spectrum of the FP cavity is shown in Fig. 1(c), and the red dashed line represents the probe laser with wavelength of 1542.7 nm. A part of light from the continuous-wave probe laser is coupled into the FP cavity through a fiber circulator (FC). Then, the reflective light from the FP cavity and the reference light with the same intensity are detected by a balanced photodetector (PD). The right inset in Fig. 1(a) shows the relative location between the SiN membrane and the SMFs, where four standard SMFs are inserted into a ceramic ferrule to read out the displacements at different location of the membrane. Compared with other SMFs, the SMF marked by a red circle is more sensitive for more mechanical modes, and thus is used in our experiments. Figure 1(d) shows the thermal Brownian noises of the membrane, where three resonant mechanical modes are observed apparently. The corresponding frequencies (Q_{mec}) of (1,1), (1,2) and (2,1) modes are 379.55 kHz (9.5×10^4), 592.145 kHz (1.5×10^5) and 608.811 kHz (1.2×10^5). The insets are the modeshapes obtained by finite-element simulations.

Compared with the sensors using high-Q optical cavities, the two-beam FP cavity offers a wider linear range for the laser wavelength (about 4 nm as shown in Fig. 1(c)), eliminating the

Optics EXPRESS

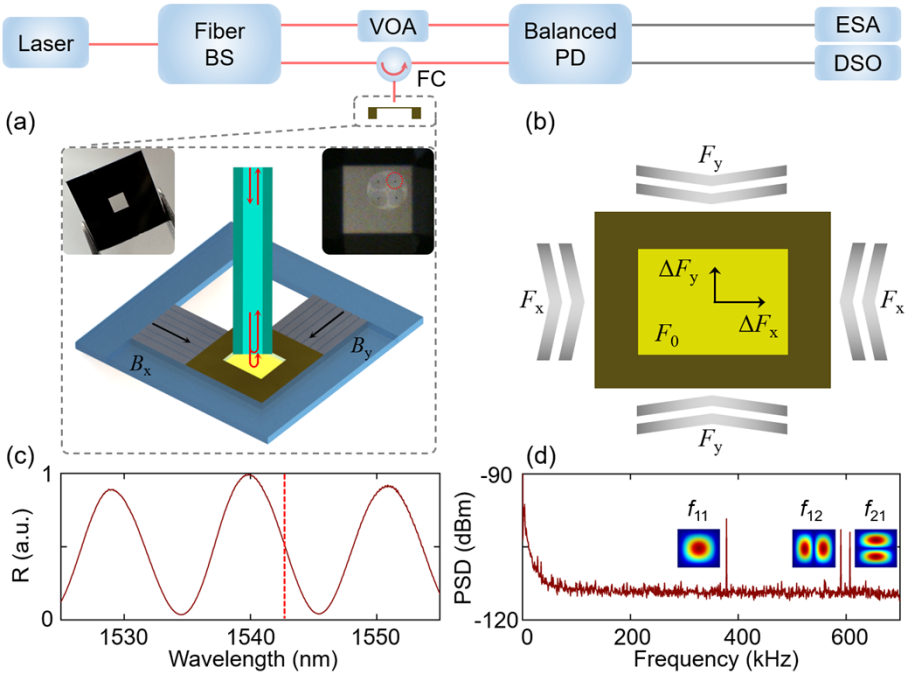

Fig. 1. Overview of the optomechanical magnetometer. (a) Schematics of the experimental setup and magnetometer. Inset: photographs of the SiN membrane (left) and the relative position between the membrane and the optical fibers (right). (b) Stress diagram of the membrane under different magnetic fields. (c) Reflective spectrum of the FP cavity and wavelength of the probe light (red dashed line). (d) Power spectral density (PSD) of thermal Brownian noise of the membrane. Inset: the modeshapes of three mechanical modes for the membrane. Fiber BS, fiber beam splitter; FC, fiber circulator; VOA, variable optical attenuator; Balanced PD, balanced photodetector; ESA, electrical spectrum analyzer; DSO, digital storage oscilloscope.

dependence of ultrasensitive optomechanical magnetometers on expensive ultranarrow-linewidth lasers and sophisticated frequency locking equipment. Meanwhile, it is also insensitive to polarization fluctuations of the probe light because the empty cavity cannot result in polarization change between the two reflective beams, removing the requirement of dedicated polarization control for the reported counterparts.

3. Results and discussion

3.1. Response to DC magnetic fields

When a DC ambient magnetic field is applied to the magnetometer, the corresponding Terfenol-D plates elongate and extrude the silicon chip, and thus change the intrinsical tensile stress of the membrane as shown in Fig. 1(b). According to Eq. (2), the change of the intrinsical tensile stress shifts the resonant frequencies of the membrane. Therefore, the DC ambient magnetic field could be obtained by demodulating the resonant frequency shifts. Figure 2 depicts the theoretical resonant frequency shifts of different mechanical modes for a rectangular SiN membrane with a size of 993μm × 1006μm × 50 nm as functions of ambient magnetic fields B_x and B_y, where the simulated parameters are $E = 270$ GPa, $\sigma_0 = 0.815$ GPa, $k = 1.95$ ppm/Gs, $L_{TD} = 50$ mm, $L_{SI} = 5$ mm, and $\rho = 2700$ kg/m^3. As the ambient magnetic fields increase, the resonant frequencies of all six mechanical modes decrease because of the reduction of the intrinsical tensile stress in

Optics EXPRESS

the membrane. Interestingly, the frequency shift of (1,2) mode is less than that of (2,1) mode when the magnetic field is in x direction, but it is not the case when the magnetic field is in y direction. Under the condition of $\Delta F_i << F_0$ and applying the Taylor expansion to the Eq. (1), we find that the frequency shift is approximately linear with the ambient magnetic field. Therefore, the amplitude and direction of the ambient magnetic field in x-y plane could be determined by the equation

$$\begin{pmatrix} B_x \\ B_y \end{pmatrix} = \begin{pmatrix} S_{12x} & S_{12y} \\ S_{21x} & S_{21y} \end{pmatrix}^{-1} \begin{pmatrix} \Delta f_{12} \\ \Delta f_{21} \end{pmatrix} \tag{5}$$

$$\overrightarrow{B} = B_x \overrightarrow{x} + B_y \overrightarrow{y} \tag{6}$$

where B_x and B_y are x and y components of the vector magnetic field B, S_{12x}, S_{12y}, S_{21x}, and S_{21y} are the shift rates of (1,2) and (2,1) mode under x and y directional magnetic fields, and Δf_{12} and Δf_{21} are frequency shifts of (1,2) and (2,1) mode under the ambient magnetic field. In addition, the shift of (3,1) mode is more than that of (2,1) mode with a x-direction magnetic field as shown in Fig. 2(a), and thus better sensitivity could be obtained by employing higher order modes, which can also be validated by Eq. (1).

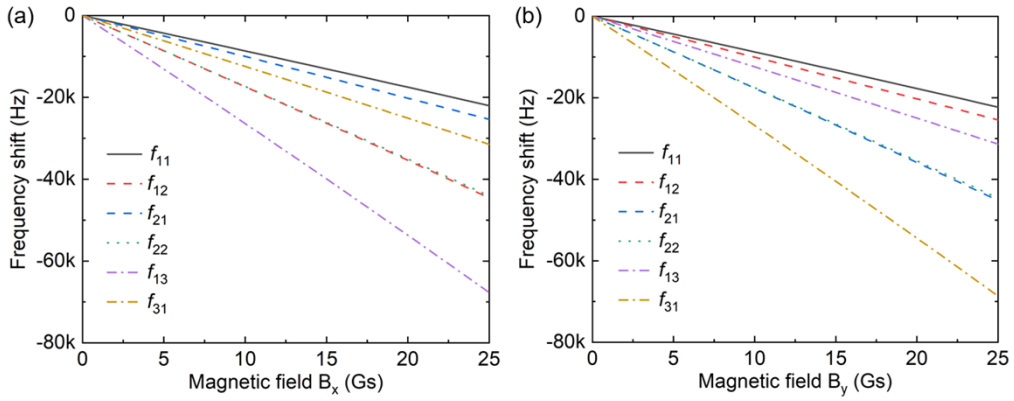

Fig. 2. Theoretical resonant frequency shifts of the six mechanical modes for the SiN membrane (993μm × 1006μm × 50 nm). (a) Frequency shifts versus the different x-directional DC magnetic fields. (b) Frequency shifts versus the different y-directional DC magnetic fields.

In our experiments, the DC magnetic fields are generated by two coils and low-noise power sources (B2961A, Keysight), and are calibrated using a commercial magnetic sensor (Mode 475, Lakeshore). Figure 3 shows the response of the (1,2) and (2,1) modes of the SiN membrane (993μm × 1006μm × 50 nm) under x-direction and y-direction DC magnetic fields, where the resolution bandwidth of the ESA is 1 Hz. Both of the resonant frequencies of the two modes decrease as the ambient magnetic fields increase, and the frequency shift rates of the two modes are different for B_x and B_y, which are consistent with the theoretical prediction. The frequency shifts vary linearly with the magnetic field when the magnetic field is less than 22 Gs. The measured shift rates S_{12x}, S_{12y}, S_{21x}, and S_{21y} are 984 Hz/Gs, 1771Hz/Gs, 1753Hz/Gs and 986 Hz/Gs. The corresponding DC magnetic-field resolutions achieved by demodulating the resonant frequency shifts [48,49], are 101.6 nT, 56.5 nT, 57.1 nT, and 101.4 nT using an ESA with a *RBW* of 1 Hz in our experiments, respectively. The resolutions could be improved further by using higher order mechanical modes as shown in Fig. 2. As the magnetic fields increase further and are more than 22 Gs, the shift rates gradually reduce because the responses of Terfenol-D plates tend to be saturation. The limitation that the responses of the Terfenol-D plates to ± x direction

Optics EXPRESS

magnetic field are same, could be solved by applying a bias DC magnetic field B_{bais}, where the mechanical resonant frequencies decrease when the ambient magnetic fields is codirectional with the B_{bais}, otherwise they increase.

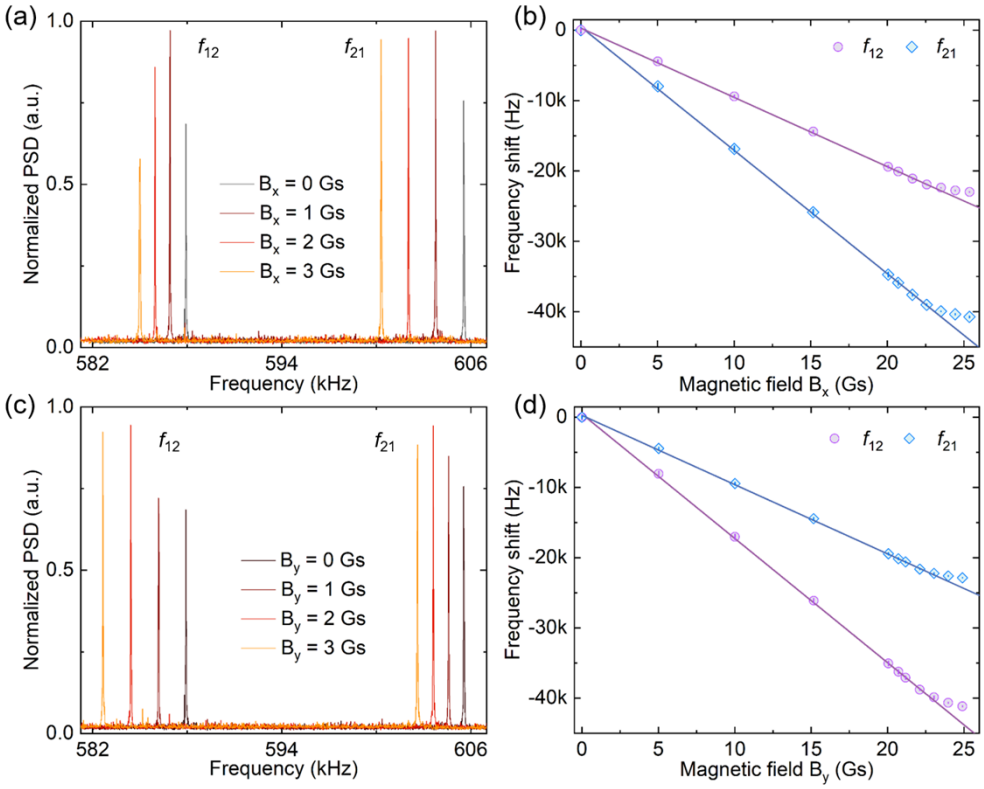

Fig. 3. Measured response of the magnetometer to DC magnetic fields. (a) PSD of thermal Brownian noises and (b) mechanical resonance frequency shifts with different *x*-directional magnetic fields. (c) PSD of thermal Brownian noises and (d) mechanical resonance frequency shifts with different *y*-directional DC magnetic fields.

3.2. Response to AC magnetic fields

We also test the response of this device to AC magnetic fields. Figure 4(a) shows the thermal Brownian noise spectra of the (1,1), (1,2) and (2,1) modes of the membrane, where the broadband spectrum has been shown in Fig. 1(d). A swept AC magnetic field with a constant amplitude of 3.4 nT is used to excite the magnetometer. The response of the magnetometer is shown in Fig. 4(b), where the resolution bandwidth *RBW* of the ESA is 3.9 Hz. The magnetic-field sensitivity B_{min} could be obtained by[36]

$$B_{\text{min}} = \frac{B_{ref}}{\sqrt{SNR \times RBW}} \tag{7}$$

where *SNR* is the ratio of the response to the thermal Brownian noise and B_{ref} is the reference exciting magnetic field. Benefiting from the mechanical resonant enhancement, the proposed magnetometer is responsive to AC magnetic fields at different frequencies, and the sensitivities at mechanical resonant modes are better than that at non-resonant frequencies. As shown in Fig. 4, the peak AC magnetic-field sensitivity is 17.9 pT/Hz$^{1/2}$ at (1,1) mode with a resonant frequency of 379.550 kHz and the sensitivities at non-resonant frequencies are at subnanotesla/Hz$^{1/2}$ level.

Optics EXPRESS

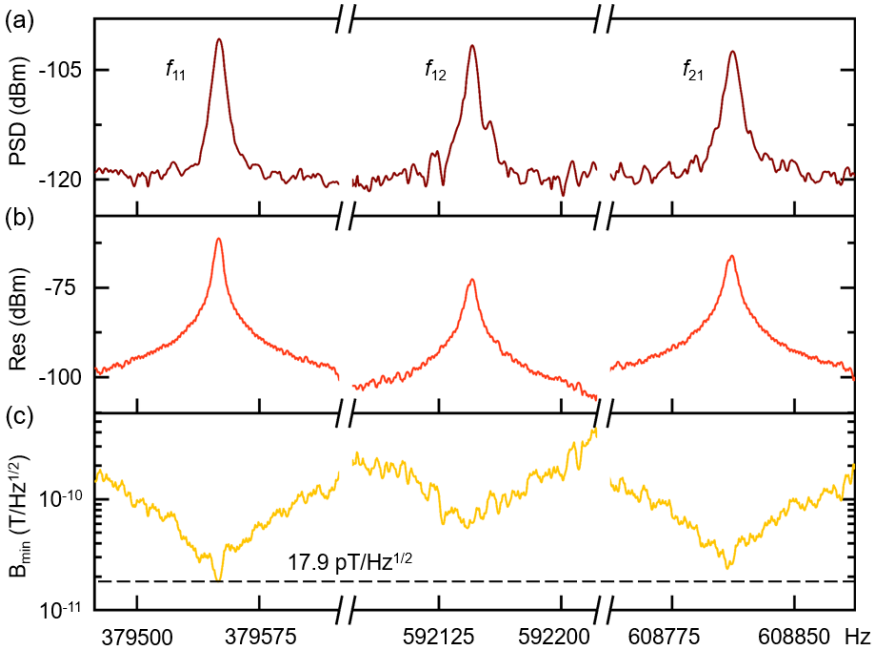

Fig. 4. Measured response of the magnetometer to AC magnetic fields. (a) Power spectral density of the thermal Brownian noise spectra of the (1,1), (1,2) and (2,1) modes. (b) Responses of the magnetometer with AC magnetic-field excitation. (c) Magnetic-field sensitivity Bmin of the magnetometer.

The observed peak DC magnetic-field resolution is 56.5 nT, which is nearly three orders of magnitude higher than the best value of 30 μT for reported magnetometers with WGM resonators by monitoring optical spectrum shift [47], and they are unsuitable for AC magnetic-field measurements due to the slow responses of optical spectrum analyzers and magnetic fluid. The DC resolution of this magnetometer could be enhanced by increasing the mode indices (m, n) and the length and magnetostrictive coefficient of the Terfenol-D plates, and decreasing the density and side lengths of the membrane resonator and the length of the silicon chip according to Equations (2)–(4). The peak AC magnetic-field sensitivity of this magnetometer could also be optimized by increasing the length and magnetostrictive coefficient of the Terfenol-D plates and using SiN membranes with higher Q_{mec}.

4. Conclusion

In summary, a unique optomechanical magnetometer based on a SiN-membrane optomechanical system is demonstrated. Benefiting from the intrinsical high tensile stress, the SiN membrane offers high-Q mechanical resonances and its resonant frequencies are highly dependent on the intrinsical tensile stress, presenting an ultrasensitive magnetic-field sensing mechanism by combining magnetostrictive materials. Simultaneous measurement of AC and DC (2D) magnetic fields with ultrahigh sensitivities is realized using only a single probe laser. Our work offers a promising candidate to measure weak magnetic fields for potential applications from mineral exploration, archaeology, geomagnetic anomalies, to space exploration missions.

Funding. National Natural Science Foundation of China (12174232, U21A6006, 11804208); Innovation Program for Quantum Science and Technology (2023ZD0300400).

Disclosures. The authors declare no conflicts of interest.

Optics EXPRESS

Data availability. Data underlying the results presented in this paper are not publicly available at this time but may be obtained from the authors upon reasonable request.

References

1. M. Aspelmeyer, T. J. Kippenberg, and F. Marquardt, "Cavity optomechanics," Rev. Mod. Phys. **86**(4), 1391–1452 (2014).
2. X. Jiang, A. J. Qavi, S. H. Huang, *et al.*, "Whispering-gallery sensors," Matter **3**(2), 371–392 (2020).
3. B. Li, L. Ou, Y. Lei, *et al.*, "Cavity optomechanical sensing," Nanophotonics **10**(11), 2799–2832 (2021).
4. X. Han, W. Fu, C. Zou, *et al.*, "Microwave-optical quantum frequency conversion," Optica **8**(8), 1050–1064 (2021).
5. B. J. Eggleton, C. G. Poulton, P. T. Rakich, *et al.*, "Brillouin integrated photonics," Nat. Photonics **13**(10), 664–677 (2019).
6. D. Mason, J. Chen, M. Rossi, *et al.*, "Continuous force and displacement measurement below the standard quantum limit," Nat. Phys. **15**(8), 745–749 (2019).
7. Y. Lai, M. Suh, Y. Lu, *et al.*, "Earth rotation measured by a chip-scale ring laser gyroscope," Nat. Photonics **14**(6), 345–349 (2020).
8. S. Tang, M. Zhang, J. Sun, *et al.*, "Single-particle photoacoustic vibrational spectroscopy using optical microresonators," Nat. Photonics **17**(11), 951–956 (2023).
9. A. Schliesser, G. Anetsberger, R. Rivière, *et al.*, "High-sensitivity monitoring of micromechanical vibration using optical whispering gallery mode resonators," New J. Phys. **10**(9), 095015 (2008).
10. A. G. Krause, M. Winger, T. D. Blasius, *et al.*, "A high-resolution microchip optomechanical accelerometer," Nat. Photonics **6**(11), 768–772 (2012).
11. S. Schreppler, N. Spethmann, N. Brahms, *et al.*, "Optically measuring force near the standard quantum limit," Science **344**(6191), 1486–1489 (2014).
12. M. Merklein, I. V. Kabakova, T. F. S. Büttner, *et al.*, "Enhancing and inhibiting stimulated Brillouin scattering in photonic integrated circuits," Nat. Commun. **6**(1), 6396 (2015).
13. F. G. Cervantes, L. Kumanchik, J. Pratt, *et al.*, "High sensitivity optomechanical reference accelerometer over 10 kHz," Appl. Phys. Lett. **104**(22), 221111 (2014).
14. V. Peano, H. G. L. Schwefel, C. Marquardt, *et al.*, "Intracavity Squeezing can enhance quantum-limited optomechanical position detection through deamplification," Phys. Rev. Lett. **115**(24), 243603 (2015).
15. W. Yu, W. Jiang, Q. Lin, *et al.*, "Cavity optomechanical spring sensing of single molecules," Nat. Commun. **7**(1), 12311 (2016).
16. M. Wu, N. L. Y. Wu, T. Firdous, *et al.*, "Nanocavity optomechanical torque magnetometry and radiofrequency susceptometry," Nat. Nanotechnol. **12**(2), 127–131 (2017).
17. J. A. Guggenheim, J. Li, T. J. Allen, *et al.*, "Ultrasensitive plano-concave optical microresonators for ultrasound sensing," Nat. Photonics **11**(11), 714–719 (2017).
18. N. S. Kampel, R. W. Peterson, R. Fischer, *et al.*, "Improving broadband displacement detection with quantum correlations," Phys. Rev. X **7**(2), 021008 (2017).
19. W. Chen, S. K. Özdemir, G. Zhao, *et al.*, "Exceptional points enhance sensing in an optical microcavity," Nature **548**(7666), 192–196 (2017).
20. S. Basiri-Esfahani, A. Armin, S. Forstner, *et al.*, "Precision ultrasound sensing on a chip," Nat. Commun. **10**(1), 132 (2019).
21. A. G. Primo, N. C. Carvalho, C. M. Kersul, *et al.*, "Quasinormal-Mode perturbation theory for dissipative and dispersive optomechanics," Phys. Rev. Lett. **125**(23), 233601 (2020).
22. Q. Zhang, R. Zhai, S. Yang, *et al.*, "Microfiber mechanical resonator for optomechanics," ACS Photonics **7**(3), 695–700 (2020).
23. T. Liu, F. Pagliano, R. V. Veldhoven, *et al.*, "Integrated nano-optomechanical displacement sensor with ultrawide optical bandwidth," Nat. Commun. **11**(1), 2407 (2020).
24. E. Gil-Santos, J. J. Ruz, O. Malvar, *et al.*, "Optomechanical detection of vibration modes of a single bacterium," Nat. Nanotechnol. **15**(6), 469–474 (2020).
25. W. J. Westerveld, M. Mahmud-Ul-Hasan, R. Shnaiderman, *et al.*, "Sensitive, small, broadband and scalable optomechanical ultrasound sensor in silicon photonics," Nat. Photonics **15**(5), 341–345 (2021).
26. Q. Zhang, J. Zhang, S. Yang, *et al.*, "Microfiber optomechanical torsion sensor," Front. Phys. **11**, 1147644 (2023).
27. J. Wang, Y. Yang, M. Li, *et al.*, "Synthetic five-wave mixing in an integrated microcavity for visible-telecom entanglement generation," Nat. Commun. **13**(1), 6223 (2022).
28. B. Li, Q. X. Lin, and M. Li, "Frequency–angular resolving LiDAR using chip-scale acousto-optic beam steering," Nature **620**(7973), 316–322 (2023).
29. T. Bagci, A. Simonsen, S. Schmid, *et al.*, "Optical detection of radio waves through a nanomechanical transducer," Nature **507**(7490), 81–85 (2014).
30. M. Sansa, M. Defoort, A. Brenac, *et al.*, "Optomechanical mass spectrometry," Nat. Commun. **11**(1), 3781 (2020).
31. P. H. Kim, B. D. Hauer, T. J. Clark, *et al.*, "Magnetic actuation and feedback cooling of a cavity optomechanical torque sensor," Nat. Commun. **8**(1), 1355 (2017).
32. T. M. Hoang, Y. Ma, J. Ahn, *et al.*, "Torsional optomechanics of a levitated nonspherical nanoparticle," Phys. Rev. Lett. **117**(12), 123604 (2016).

Optics EXPRESS

33. R. Niu, M. Li, S. Wan, *et al.*, "kHz-precision wavemeter based on reconfigurable microsoliton," Nat. Commun. **14**(1), 169 (2023).
34. A. Zalogina, P. Tonkaev, A. Tripathi, *et al.*, "Enhanced five-photon photoluminescence in subwavelength AlGaAs resonators," Nano Lett. **22**(10), 4200–4206 (2022).
35. S. Forstner, S. Prams, J. Knittel, *et al.*, "Cavity optomechanical magnetometer," Phys. Rev. Lett. **108**(12), 120801 (2012).
36. C. Yu, J. Janousek, E. Sheridan, *et al.*, "Optomechanical magnetometry with a macroscopic resonator," Phys. Rev. Appl. **5**(4), 044007 (2016).
37. B. Li, J. Bilek, U. B. Hoffm, *et al.*, "Quantum enhanced optomechanical magnetometry," Optica **5**(7), 850–856 (2018).
38. J. Zhu, G. Zhao, L. Savukov, *et al.*, "Polymer encapsulated microcavity optomechanical magnetometer," Sci. Rep. **7**(1), 8896 (2017).
39. M. F. Colombano, G. Arregui, F. Bonell, *et al.*, "Ferromagnetic resonance assisted optomechanical magnetometer," Phys. Rev. Lett. **125**(14), 147201 (2020).
40. B. Li, G. Brawley, H. Greenall, *et al.*, "Ultrabroadband and sensitive cavity optomechanical magnetometry," Photonics Res. **8**(7), 1064–1071 (2020).
41. F. Gotardo, B. J. Carey, H. Greenall, *et al.*, "Waveguide-integrated chip-scale optomechanical magnetometer," Opt. Express **31**(23), 37663–37672 (2023).
42. G. Xu, Z. Shen, Y. Wang, *et al.*, "Optomechanical magnetometry on a bubble resonator with YIG microsphere," IEEE Photonics Technol. Lett. **35**(7), 393–396 (2023).
43. Z. Hu, Y. Gao, J. Liu, *et al.*, "Picotesla-sensitivity microcavity optomechanical magnetometry," Light Sci. Appl. **13**(1), 279 (2024).
44. A. Xu, Y. Li, X. Li, *et al.*, "Subpicotesla optomechanical magnetometry," Phys. Rev. Lett. **133**(15), 153601 (2024).
45. D. Budker and M. Romalis, "Optical magnetometry," Nat. Phys. **3**(4), 227–234 (2007).
46. M. Zhuang, J. Huang, and C. Lee, "Simultaneous measurement of DC and AC magnetic fields at the Heisenberg limit," Phys. Rev. Appl. **13**(4), 044049 (2020).
47. X. Zhao, J. Song, B. Duan, *et al.*, "Research on magnetic field sensing based on whispering gallery modes microbubble resonator," Sci. Sin.-Phys. Mech. Astron. **53**(11), 114208 (2023).
48. M. S. Hanay, S. Kelber, A. K. Naik, *et al.*, "Single-protein nanomechanical mass spectrometry in real time," Nat. Nanotech. **7**(9), 602–608 (2012).
49. M. S. Hanay, S. I. Kelber, C. D. O'Connell, *et al.*, "Inertial imaging with nanomechanical systems," Nat. Nanotech. **10**(4), 339–344 (2015).